International Journal of Innovative Scientific & Engineering Technologies Research 14(3):263-290, July-Sept, 2026

© SEAHI PUBLICATIONS, 2026 www.seahipublications.org ISSN: 2360-896X

DOI:10.5281/zenodo.23118289

Synthesis And Characterization Of Al_2O_3 Nanoparticle Loaded-Rice Husk Activated Carbon For Removal Cd^{2+} Of Aqueous Solution

Ashiru Auwal Mairuwa[1]; Ikechukwu Alisi Ogadimma[2]; Sadiq Sani[3]

[1]Al-Qalam University Katsina, State, Nigeria.
Email: ashiruauwalmairuwa15@gmail.com

[2,3] Federal University Dutsin-ma, Nigeria
Email: ialisi@fudutsinma.edu.ng
Email: ssani@fudutsinma.edu.ng

ABSTRACT

This research aimed to synthesize and characterize Al_2O^{3-} loadedd-rice husk activated carbon for removal of Cd^{2+} from aqueous solution. Al_2O_3-loaded rice husk activated carbon nanocomposites was synthesized, charcterized and evaluated by chemical and hydro thermal method for the adsorption of Cd^{2+} from aqueous solutions using experimental design and optimization. Characterization confirmed successful nanoparticle incorporation, with the Al_2O_3 nanocomposite exhibiting higher surface area and more active sites which resulted in superior adsorption performance. Optimization using Central Composite Design showed that adsorbent dosage, initial metal ion concentration, pH, and contact/sonication time significantly affected metal removal. Maximum removal efficiencies of about 92.4% for Cd^{2+} on Al_2O_3 was achieved under optimal conditions. Adsorption equilibrium followed the Langmuir model (R^2>0.99) indicated monolayer adsorption, with maximum capacities of 166.7 mg g^{-1} (Cd^{2+}/Al_2O_3). Kinetic data were best described by the pseudo-second-order model (R^2 0.99) suggested chemisorption, while intra-particle diffusion contributed at later stages. Thermodynamic analysis confirmed that adsorption was spontaneous and endothermic, with negative ΔG°, positive ΔH°, and positive ΔS° values.

Keywords: Al2O3 nanocomposite, Rice husk activated carbon, Cd^{2+} removal,Optimization, Isotherm, Kinetics, Thermodynamics, Wastewater treatment

INTRODUCTION

Heavy metal contamination in wastewater poses serious environmental and public health risks due to their toxicity, persistence, and non-biodegradable nature. Cadmium (Cd^{2+}) is particularly hazardous and toxic metal which can accumulate and cause serious health and environmental problems (Rajput and Yaning, 2023).

The rice husk is the covering obtained after the milling process carried out on the rice grain. The husk is the outermost covering on the rice grain and makes us 20–25% of the grains' total weight (Dickin et al., 2017). After the milling, disposal of the husk becomes a major challenge in many areas and as such end up being burnt or discarded indiscriminately, causing lots of environmental pollution (Ramasamy, 2021).

Loading activated carbon with nanoparticles has attracted a lot of attention as a means of modification because nano-composites combine the individual properties of the nanoparticles and activated carbon leading to an adsorbent with enhanced adsorptive capacity (Rafatullah et al., 2019). Among the types of nanoparticles, metal oxides vis-à-vis core-shell zerovalent iron, manganese oxide, zinc oxide, titanium oxide, copper oxide and cesium oxide have been reported as operational adsorbents for pollutants' removal owing to their uniqueness in terms of surface area, selectivity, and ability to penetrate the contamination zone of pollutants (White et al 2019).

They possess a lot of matrices or stabilizers to obtain hybrid nano-composite adsorbents (Mubita et al., 2019). These nanocomposites have shown the ability to increase the sorption capacity of the adsorbents to which it is loaded. Nano-composites have exhibited efficiency in the sorption of various pollutants such as pharmaceuticals, dyes and heavy metals (Ekpete et at., 2020).

Equally, these nanocomposites have been shown to have reusability capacity without a drastic or ridiculous reduction in the efficiency of the adsorbent (Masoudian et al., 2019)

Undoubtedly, activated carbon stands in the forefront of the full line of adsorbents. The growing interest in this material is motivated by its favorable surface properties, uniformity of adsorption, and consequently exceptional adsorption effect. In addition, this material is relatively cost-effective compared to other inorganic adsorbent such as zeolites (Mjin et al., 2018)

Optimization analysis automates the manual procedure for a particular configuration. Trends are detected quickly and the optimum solution is identified in the fewest number of test runs (Ahmed, 2019).

MATERIALS AND METHOD

Equipments and Chemicals

Beaker,Wash bottles, Analytical weighing balance(BA2204N), Mortar and pestle, Test tubes, Crucible, Desicator, Oven (DHG-9023A), Muffle furnace(SX-25-10), pH Meter (SN:201811083), Autoclave machine (SX-25-10), Centrifuge machine (800D), XRD Machine (Buker D8), FESEM EDXMachine (JSMIT810), FTIRMachine (IRTracer100), TGAmachine (TGA550), BETanalyzer (HORIBA SA-9650), Magnetic stirrer, Ethanol (50%), Nitric acid (1.0 M HNO3), Deionised water, Rice-husk, Sodium hydroxide (1.0 M NaOH), Phosphuric acid (I.0 M H3PO4), Zinc acetate (Qualikems Fine Chem Pvt. Ltd), Aluminium sulphate (Qualikems Fine Chem Pvt. Ltd), Lead(ll)chloride (Guangdong Guanghua Sc-Tech Co., Ltd), Cadmium (ll) chloride (Guangdong Guanghua Sc-Tech Co., Ltd), AAS Machine (AA320N)

Preparation of Reagents

Preparation of 1.0 M Nitric (HNO3) Acid

HNO3(1.0 M) acid was prepared by diluting 66.7ml concentrated HNO3 acid in 500 ml distilled water inside 1000 volumetric flask, later the volumetric flask was raised to the mark with distilled water (Fraser, 2022).

Preparation of 1.0 M and 0.2 M Sodium Hydroxide (NaOH)

NaOH (I.O M) was prepared by dissolving 40 g NaOH pellet in 500 ml distilled water inside 1000 volumetric flask, later the volumetric flask was raised to the mark with distilled water.

NaOH (0.2 M) was prepared by dissolving 8 g NaOH pellet in 500 ml distilled water inside 1000 volumetric flask, later the volumetric flask was raised to the mark with distilled water (Gilchrist, 2019).

Preparation of 1.0 M Phosphoric (H3PO4) Acid

H3PO4(1.0 M) acid was prepared by diluting 68.5 ml concentrated H3PO4 acid in 500 ml distilled water inside 1000 volumetric flask, later the volumetric flask was raised to the mark with distilled water (Leddy et al., 2018).

Preparation of Waste Water (Cd2+ ion Solution)

Stock solution (1000 ppm) of Cd2+ ion was prepared by dissolving 1.630 g of CdCl2 in 500 ml disctilled water inside 1000 volumetric flask, which later the Flask was raised to the mark with

distilled water. Various concentrations (100 ppm, 300 ppm, 500 ppm, 700 ppm and 900 ppm) were also prepared by measuring 100 ml, 300 ml, 500 ml, 700 ml and 900 ml from the stock solution and diluted to the mark of 1000 size volumetric flask with distilled water resapectively (Mahmood and Malik 2019).

Sample Collection and Preparation

The Rice husk (RH) was obtained from local farmers in Dutsin-Ma Local Government Area, Katsina State, Nigeria. It was screened and thoroughly washed to remove impurities and dust. With the aid of distilled water, the rice husk was rinsed and oven-dried for 3 hrs at 110°C. About 1200 g of the rice husk was treated with 3000 mL 1.0 M HNO_3 acid at (1:3 ratio) to remove metallic impurities, rinsed and dried, and then treated with 1.0 M NaOH to remove silica content and brick red coloured RH was obtained (Dada et al., 2022). Subsequently, it was transferred to a furnace for carbonization at 400 °C over an hour.

Carbonization and Chemical Activation

Treated RH (1200 g) was measured into 2000 mL beaker containing 1.5 Litre 1 M H_3PO_4. The contents was transferred in to crucible and heated at 70 °C for about 10 h until a paste was formed. The paste in the crucible was heated at 400 °C in a muffle furnace over 1 hour. The resulting rice husk activated carbon (RHAC) was cold and thoroughly rinsed with de-ionized water to obtain a neutral pH solution a using pH meter (Dada et al., 2022). The activated carbon was oven-dried at 105 °C and labelled as RHAC which was kept in a desiccator (air-tight) for further utilization.

Synthesis of Aluminium Oxide Nanoparticles

Aluminium Sulphate (504.3 g) was dissolved in 2 Litre distilled water to prepare 0.1 M Aluminium Sulphate, and the solution was then preserved under constant stirring for an hour. After the complete dissolution of the Aluminium Sulphate, 1 Litre 0.2 M NaOH solution was added. The white creamy solution was left to settle overnight, and then, the supernatant was carefully discarded. The precipitate was washed several times using distilled water and dried overnight at 80 °C. Complete conversion of Aluminium hydroxide into alumina during drying was attained (White et al., 2020).

Synthesis of Al_2O_3-Activated Carbon Nanocomposite

Approximately, 100 g of activated carbon was mixed with 20 g of Al_2O_3 powder. The mixture was added with ethanol to completely immerse. The mixture was slowly stirred with magnetic stirrer while slowly heating for 2 hours until the ethanol volume decreased. After cooling down, the mixture was washed with distilled water for few times and left overnight. The mixture was dried in an oven for 1 h at 110 °C. Dried mixture was placed into the hydrothermal reactor. The temperature was slowly increased to 250 °C for 3 hours (Efome et al., 2018). After cooling down, the composite was taken up from hydrothermal reactor and washed for few times to reduce ash content. Finally, the Composite was dried in an oven at 110 °C over an hour.

Characterization Techniques

XRD Analysis

X-ray diffraction (XRD) analysis was conducted to determine to investigate the structure and crystallinity of the Al_2O_3 and ZnO nanoparticles. The crystallite size of the synthesized $Al_2O_3$and ZnO nanoparticles and nanocomposite was measured by this analysis (Alipanahpour et al., 2019)..

FESEM-EDX Analysis

Field emission scanning electron microscopy with energy-dispersive X-ray spectroscopy was used to study and analyze the surface morphology of the adsorbent and their elemental composition respectively before and after adsorption (optimization). The materials were subjected to analysis before and after the adsorption of the heavy metal ions (Qadir et al., 2020).

FTIR Analysis

The variation in the vibration frequency of functional groups before and after activation process was measured using Fourier transform infrared (FTIR) spectroscopy. Infrared spectra were recorded within the range of 550–4000 cm^{-1}. Essential FTIRv3.5 was used to process and analyze the spectral data (Shakir et al., 2017).

BET Analysis

The average particle size and narrow distribution range of Al2O3 and ZnO nanoparticles and nanocomposite was measured and analyzed by BET analyzer (HORIBA SA-9650) (Mahmood and Malik 2019).

TGA Analysis

The multi-stage weight loss and temperature change of Al2O3 and ZnO nanoparticles and nanocomposite was measured and analyzed TGAmachine (TGA-550) (Shakir et al., 2017).

Optimization for heavy Metals Removal from Waste Water.

Adsorption experiments were carried out in the batch mode by optimizing different parameters: solution pH (3–11), sonication time (10–50 min), adsorbent dosage (0.2 – 1.0 g), initial metal ion concentration (100–900 mg/L). The pH values of all the solutions were adjusted by adding 1.0 M HNO3 acid or 1.0 M NaOH solution. A measured amount of metal ion sample (100 mL) and a given amount of the adsorbent would be taken into 250 mL conical flask for batch experiment and agitated with magnetic stirrer on digital hot plate at 200 rpm. The solids would be separated through filtration by using Whatman 42 filter paper. At the end of each experiment, small amounts of the solutions (supernatants) were withdrawn at predetermined time, and the heavy metal ion concentration in the filtrate was determined using AAS (Atomic Absorption Spectrophotometer). Experiments were carried out in triplicate and mean values were used (Shakir et al., 2017).

The percentage removal of metal ion (metal ion removal efficiency) (%) or % adsorption was obtained using equation (2.1), while, the equilibrium adsorption capacity was calculated using equation (2.2) (Ahmed, 2019).

$$\text{Metal ion removal efficiency (\%)} = \frac{C_o - C_e}{C_n} \times 100 \qquad 2.1$$

$$\%(mg/g) = \frac{(C_o - C_e)V}{m} \qquad 2.2$$

Where is the equilibrium adsorption capacity , is the initial metal ion concentration (mg/L), is the liquid-phase concentrations of the metal ion (mg/L) at equilibrium, V is the volume (L) of the meta ion solution (adsorbate), and m is the mass (g) of the adsorbent.

Application of response surface methodology (RSM) based on the central composite design (CCD) was used to study the effects of four various parameters including metal ion concentration, the amount of adsorbent, sonication time and pH on the process of adsorption (Table 2.1).

As presented in Table 3.1, the complete design would consist of 30 runs which would be done randomly. The model of the adsorption process is explained by the following quadratic equation:

$$Y = \beta_0 + \sum_{i=1}^{k} \beta i + Xi + \sum_{i=1}^{k} \beta ii\ X^2 i + \sum_{i=1}^{k} \sum_{j=1}^{k} \beta ij\ x\ i\ x\ j + E \qquad 2.3$$

Where Y is the predicted response function (% Removal), and ε are constant and error terms respectively, and are the coded values of our independent parameters, is the linear coefficient, is the quadratic coefficient and is the interaction coefficient.

Table 2.1: Central Composite Design Factors and Levels for the Adsorption of Pb^{2+} and Cd^{2+} by Al_2O_3 and ZnO Nanoparticle-loaded with Rice Husk Activated Carbon

Factors	**Code**	**Unit**	**Levels**				
			1	2	3	4	5
Amount of Adsorbent	A	G	0.2	0.4	0.6	0.8	1.0
Metal ion Concentration	B	mg/L	100	300	500	700	900
P^H	C		3	5	7	9	11
Sonication Time	D	Min	10	20	30	40	50

The factor levels would be coded as –α (lowest), -1 (low), 0 (middle), 1 (high) and +α (highest).
Volume of metal ion solution to be used = 100 mL
The pH of the solution was adjusted by adding 1.0 M HNO3 acid or 1.0 M NaOH solution.
Where Co and Cf (in mg/L) are the initial and final concentrations of the metal ion in aqueous solution respectively,

3.11. Adsorption Isotherm

Equilibrium data are often referred to as adsorption isotherms. They are the basic requirements for the design of adsorption systems. Equilibrium study on adsorption can provide information on the adsorption capacity of the adsorbent. The various constant values that characterize the adsorption isotherm express the surface properties and affinity of the adsorbent. They could be used to compare the adsorptive capacities of the adsorbent for different substances, such as pollutants (Ojediran et al 2020).

The adsorption Isotherms of heavy metal ion adsorption on to Al2O3 and ZnO Nanoparticles-loaded with Rice Husk Activated Carbon was studied using the Langmuir, Freundlich andTemkin isotherm models. These adsorption models were used to describe the equilibrium between metal ions and adsorbent at constant temperature. Coefficients of determination ( ) were calculated for the considered isotherm models to indicate the extent of agreement between the experimental values and isotherm parameters, and also to confirm or reject the monolayer metal ion on Al2O3 and ZnO Nanoparticles-loaded Rice Husk Activated Carbon (Okewale and Omoruwuo 2018).

Langmuir isotherm

The Langmuir isotherm specified monolayer adsorption of the metal ion onto the surface containing a finite number of identical sites. The model is based on the assumption that adsorption takes place at specific homogeneous sites within the adsorbent and there is no interaction between the adsorbed species (Okewale and Omoruwuo 2018).

The linear form of the Langmuir model equation is presented in Equation (2.4).

$$\frac{1}{\%} = \left(\frac{1}{q_{max}}\right) + \frac{1}{b q_{max} C_e} \qquad 2.4$$

Where,C_e (*mg/L*) is the equilibrium concentration of the adsorbate,q_e (*mg/gm*) is the amount of adsorbate adsorbed per unit mass of adsorbent (adsorption capacity), at equilibrium,q_{max} (*mg/gm*) and *b* (*L/mg*) are Langmuir constants related to maximum monolayer adsorption capacity of the adsorbent and energy of adsorption respectively.

The values of $q_{max}$and *b* were calculated from the slope and intercept of plot of $\frac{1}{q_e}$against $\frac{1}{C_e}$ respectively ((Ahmed, 2019). The main features of the Langmuir isotherm model may be expressed in terms of equilibrium parameter R_L which is a dimensionless constant referred to as separation factor or equilibrium parameter. R_L , can be calculated using Equation (2.5)

$$R_L = \frac{1}{1+bC_o} \qquad 2.5$$

Where, C_0(mg/L) is the initial concentration of adsorbate and b (L/mg) is the Langmuir constant described above.

Freundlich isotherm

The Freundlich isotherm model assumed that the adsorption takes place on heterogeneous surfaces which have different adsorption energies (multilayer adsorption) (Ahmed, 2019).

The model has the following form (Equation 2.6):

$$q_e = K_f C_e^{\frac{1}{n}} \quad 2.6$$

Where C_e is the equilibrium concentration of adsorbate (*mg/L*),$K_f$and *n* are Freundlich parameters related to the extent of adsorption(adsorption capacity) and the intensity of adsorption respectively. The constants $K_f$and *n* can be obtained by taking *log* on both sides of equation (3.7) as presented in Equation 6 and plotting $\log q_e$against $\log C_e$.The value of n and K_f can be obtained from the slope and the intercept of the linear plot.

$$\log q_e = \log k_f + \frac{1}{n} \log C_e \quad 2.7$$

Temkin isotherm

The Temkin isotherm model was used to describe the adsorption of heavy metals onto Al_2O_3 and ZnO nanocomposite-loaded rice husk activated carbon, assuming a linear decrease in heat of adsorption with surface coverage.

The linear form is given as:

$$q_e = B\ln A + B\ln C_e \quad 2.8$$

where qe (mg/g) is the amount of metal ions adsorbed at equilibrium, Ce (mg/L) is the equilibrium concentration, A (L/g) is the Temkin equilibrium binding constant, and B=RT/b, with R as the universal gas constant (8.314 J/mol•K), T (K) as the absolute temperature, and b as the Temkin constant related to heat of adsorption.

Experimental data were fitted by plotting qe against lnCe. The constants were obtained from the slope and intercept, while the model suitability was evaluated using the correlation coefficient (R^2). The parameters indicated the interaction between the adsorbent and metal ions.

Adsorption Kinetics (Kinetic Study)

The study of adsorption kinetics is of great significance in the design and modeling of efficient adsorption operations (Ahmed, 2019). Kinetic analysis is essential for understanding the adsorption process. This could be attributed to the fact that sufficient residence time on the absorber surface is needed to complete the adsorption reaction. Kinetic models were exploited to test the experimental data and to find the mechanism of adsorption and its potential rate-controlling step that includes mass transport and chemical reaction (Masoudian et al., 2019). Kinetic experiments was conducted at the optimal conditions of adsorbate pH, adsorbent dose, initial metal ion concentration, at room temperature and contact time 20–120 minutes for all adsorbents. In the adsorption kinetics, the pseudo-first-order and pseudo-second-order models were applied to the experimental data to evaluate the bio-adsorption kinetics of the metal ions. The applicability of these kinetic models was determined by measuring the correlation coefficients ( ) and the experimental value. In order to further understand the characteristics of the adsorption process, the pseudo-first-order and pseudo-second-order kinetic models was applied (Masoudian et al., 2019).

The experimental adsorption data was analyzed using three kinetic models. These models include: 1) Lagergren's pseudo-first order law; 2) McKay and Ho's pseudo-second-order law, and 3) the intra-particle diffusion model (Li et al., 2017).

The Lagergren pseudo-first order law is defined by equation (3.9). This model is conceptualized on the capacity of adsorbents for dye uptake. It also assumes that the absorption on the sorption sites depends on the empty, i.e., un-occupied adsorbents site (Li et al., 2017).

$\ln(q_e - q_t) = \ln q_e - k_1 \frac{t}{q_t}$ 2.9

Where,

q_t (mg/g) is adsorption at time t.

q_e is adsorption at equilibrium.

k_1 ($\min^{-1}$) is the pseudo-first order adsorption rate constant. The rate constant is estimated by plotting $\ln(q_e - q_t)$ against t. The applicability of the pseudo-first order kinetic model is suggested by a straight line plot of $\ln(q_e - q_t)$ versus t and q_e and k_1 was determined from the intercept and slope of the plot, respectively.

The McKay and Ho's pseudo-second-order law is described by Equation (2.10). The rate of pseudo-second-order reaction depends on the amount of adsorbed solution, the surface of adsorbent and the amount of adsorption at the equilibrium (Li *et al*., 2017). According to Li *et al*, (2017), the Pseudo-second-order model presumes that metal ion is removed through chemosorption and physisorption.

$\frac{t}{q_e} = \frac{1}{K_e q_e^2} + \frac{1}{q_e} t$ 2.10

Where k_2 (g/min.mg) is the pseudo-second-order rate constant for adsorption. It is estimated from a linear plot of $\frac{t}{q_t}$ against t.

It was observed that the adsorption process is not a single step event, but instead involves a number of steps. The first step involves diffusion of sorbate from the aqueous solution to the absorber surface. This is followed by the much slower diffusion of sorbate into the internal porous voids of the absorber matrix. This multi-step process was described using an intra-particle diffusion model which is described by Equation (2.11) (Maji, 2018).

$q_t = K_{id} t^{1/2} + C$ 2.11

Where, k_{id} is the rate constant for intra-particle diffusion estimated from plotting q_t versus $t^{1/2}$, C is the intercept that provides the ideal boundary layer thickness.

Adsorption Thermodynamics

In order to investigate the effect of temperature on the uptake of heavy metal ions, the batch experiments was acrried out at different temperatures (From the results conducted on the effect of temperature on adsorption (isothermal study), the thermodynamics of the adsorption process was investigated with the aid of various parameters such as free energy change (ΔG^o), enthalpy change (ΔH^o) and entropy change (ΔS^o). These parameters were calculated using Equations (2.12-2.15) (Atieh *et al*., 2017).

$DG^o = RT\ln K_e$ 2.12

$K_c = \frac{C_{ad}}{C_e}$ 2.13

$DG^o = DH^o - TDS^o$ 2.14

$\ln K_e = \frac{DS^o}{R} - \frac{DH^o}{RT}$ 2.15

Where,K_c is the equilibrium constant,C_{ad} is the amount of metal ion adsorbed per litre of the solution at the equilibrium,C_e is the equilibrium concentration (*mg/L*) of the metal ion in the solution, *T* is the temperature in Kelvin and *R* is the gas constant (*8.314 J/mol*).The values of ΔH^oandΔS^o was determined from the slopes and intercepts of the plot of $\ln K_c$against $\frac{1}{T}$respectively. A negative Gibbs free energy,ΔG^oindicates that the adsorption is feasible.

RESULT AND DISCUSSION

Evaluation of the percentage yield of activated carbon, metal oxide nanoparticle (Al_2O_3), and their respective nanocomposites (Al_2O_3–AC) was shown in (Table 3.1) based on the initial biomass and final product obtained.

The preparation of activated carbon from 1200 g of biomass yielded 226.7 g of product which corresponded to a 19% yield. The low yield was attributed to significant mass loss during carbonization and activation due to the removal of moisture and volatile components.

The synthesis of Al_2O_3 nanoparticles resulted in 25 g from 504.3 g of precursor and corresponded to a very low yield (5%), which was attributed to extensive decomposition and material loss during calcination.

However, the Al_2O_3-AC nanocomposite exhibited the highest yield of 91%, as 108.9 g was recovered from 120 g of precursor. This confirmed effective incorporation of Al_2O_3 into the activated carbon matrix with minimal loss.

Therefore, the results showed that nanocomposite formation was more material-efficient than standalone nanoparticle synthesis whose efficiency was improved for practical applications.

Analysis of XRD

Figure 3.1.0 showed overlaid XRD patterns of Al_2O_3 nanoparticles (Al_2O_3 NPs) and Al_2O_3 nanocomposite (Al_2O_3 NCs). The diffraction pattern of Al_2O_3 nanoparticles exhibited distinct and sharp peaks at characteristic 2θ positions thereby ascertaining the formation of crystalline aluminium oxide. The prominent reflections corresponded to the typical crystal planes of Al_2O_3 indicated good crystallinity and phase purity with no additional impurity peaks observed. This analysis suggested successful synthesis of pure nanoparticles. The relatively narrow peak widths further confirmed nanometer-scale crystallite size as estimated using the Debye–Scherrer equation.

By taken all together, the nanoparticles demonstrated higher crystallinity and sharper peaks, whereas the nanocomposite showed reduced crystallinity, peak broadening, and an amorphous background. These differences confirmed the successful incorporation of Al_2O_3 nanoparticles into the activated carbon matrix and the formation of the nanocomposite structure.

Table 3.1 Yield of Nano Particles and Nanocomposite

Nanoparticle	Biomass(g)	Product(g)	Percentage yield (%)
Activated carbon	1200	226.7	19
Al_2O_3	504.3	25	5
Al_2O_3 –AC	120	108.9	91

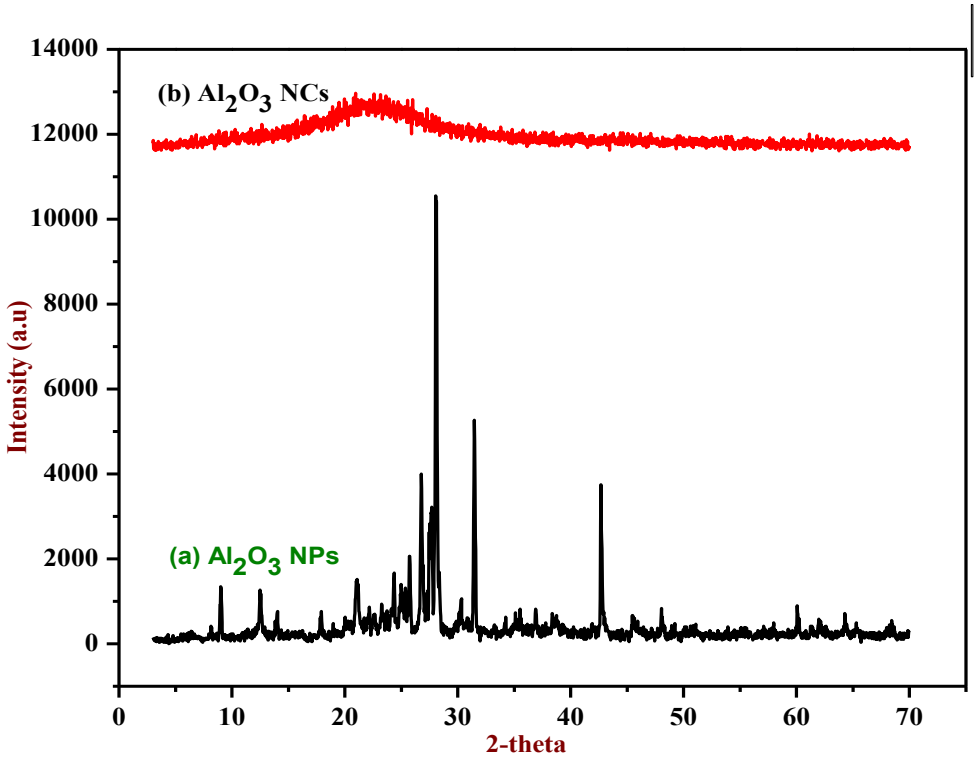

Figure 3.1.0 Overlaid XRD Patterns of (a) Al2O3 Nanoparticles (b) Al2O3 Nanocomposite

Analysis of SEM-EDX

Fig.3.2a. Showed that Al2O3 nanocomposite before adsorption has features or structures that were on the order of tens to hundreds of micrometers in size. Al2O3 Nanocomposite was likely to be a solid material with a relatively flat surface, given the high magnification and working distance.

The SEM imaging conditions (15 kV, 7.364 mm working distance, and 60 Pa chamber pressure) were optimized for high-resolution imaging of the surface and features of Al2O3 Nanocomposite.

The SEM image (Figure 3.2a) revealed irregularly shaped agglomerates with a rough and porous surface morphology. The appearance of cracks, cavities, and fractured regions indicated a heterogeneous structure with high surface roughness. Such features were significants for adsorption, as they provided abundant active sites and facilitated ion diffusion. The prevalence of smaller particles attached to larger clusters suggested nanoparticle aggregation, which was typical of Al_2O_3-based composites. Overall, the morphology confirmed a porous and irregular surface architecture, consistent with materials designed for adsorption and catalytic applications

The SEM micrographs of the Al_2O_3 nanocomposite after adsorption of Cd^{2+} uptake in (Fig.3.2c.) displayed important surface modifications compared to the pristine sample. The initially well-defined porous structure appeared coated with irregular deposits, accompanied by increased surface roughness, particle agglomeration, and partial pore blockage. In some regions, nodular or film-like layers were visible, indicating localized accumulation of Cd species. These morphological changes indicated that adsorption occured predominantly through surface complexation, complemented by possible surface

precipitation, which reduced accessible active sites and contributed to the decline in surface area after adsorption

By taken all together, SEM analysis for Al_2O_3 showed significant morphological changes after Cd^{2+} adsorption, shifting from porous, irregular pristine structures to roughened surfaces with deposits and partial pore blockage.

Elemental composition of pristine and metal-ions-loaded with Al_2O_3 was shown (Table 3.2.) Pristine Al_2O_3 contained mainly C, Si, and N, with traces of Al, consistent with its rice husk-derived silica–carbon matrix. For Cd^{2+} adsorption, Cd was detected at 0.41% on Al2O3, with the latter also showing reduced Al content, suggesting partial ion exchange or surface coverage. These results verified effective adsorption of Cd^{2+} on Al2O3 with marginally higher affinity.

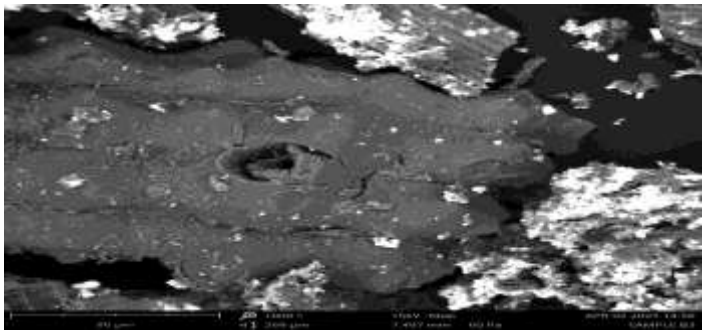

(3.2a)

Fig 3.2a SEM/EDX for Al2O3 and Fig 3.2c SEM/EDX ZnO Nano Composite Before and After Adsorption

Table 3.2. EDX/SEM for Al_2O_3 and ZnONanocomposite Before and After adsorption of Pb^{2+} and Cd^{2+}

Adsorbent	C	Si	Zn	N	Na	P	Al	Fe	K	S	Ti	Cl	Mg	Ca	Mn	Pb	Cd
A_2O_3	63.02	24.21	-	11.11	0.17	-	0.71	-	0.10	0.37	-	-	0.04	0.28	-	-	-
Al2O3-Cd^{2+}	63.25	26.78	-	9.64	0.22	-	0.10	-	-	-	-	-	-	-	-	-	0.41

Analysis of FTIR

The FTIR spectrum in (Fig. 3.3.0) testified that the rice husk activated carbon contained various functional groups, mainly hydroxyl (–OH), carbonyl (C=O), aliphatic C–H, and silicate (Si–O) groups. The Oxygenated functional groups increased the surface polarity and provided active adsorption sites made the material effective for removing dyes, heavy metals, and other pollutants. The silica-related bands also highlighted the unique composition of rice husk, which differentiated it from other biomass-derived carbons. Therefore, the FTIR results suggested that the rice husk activated carbon was chemically activated and has varous surface functionalities beneficial for adsorption processes.

The FTIR spectrum for Al_2O_3 nanocomposite in (Fig.3.3.1) range 4000–650 cm^{-1} showed that the main bands visible on the plot are approximately at 2944, 2780, 1871, 1703, 1500, 1102, 908, 808, and 780 cm^{-1}:

From 2944–2780 cm^{-1} (weak) –C–H is stretching of $–CH_2$/$–CH_3$ groups. These usually arise from residual organic precursors or capping agents (e.g., solvents, surfactants, polymer binders) left on the alumina surface.

FFrom 1703 cm^{-1} (distinct) –C=O is stretching of carbonyl groups (carboxylic/ester/ketone) from residual acetate/nitrate/organics; can also include contributions from adsorbed CO_2 species on basic Al–O sites.

From 1500–1650 cm^{-1} (weak to moderate) –H–O–H is bending from adsorbed water and/or aromatic/olefinic C=C vibrations if an organic component is part of the composite.
From 1102 cm^{-1} – Framework Al–O (and Al–O–H/Al–O–Al) vibrations; in AlOOH/γ-Al_2O_3 this band often appears near 1050–1120 cm^{-1}.

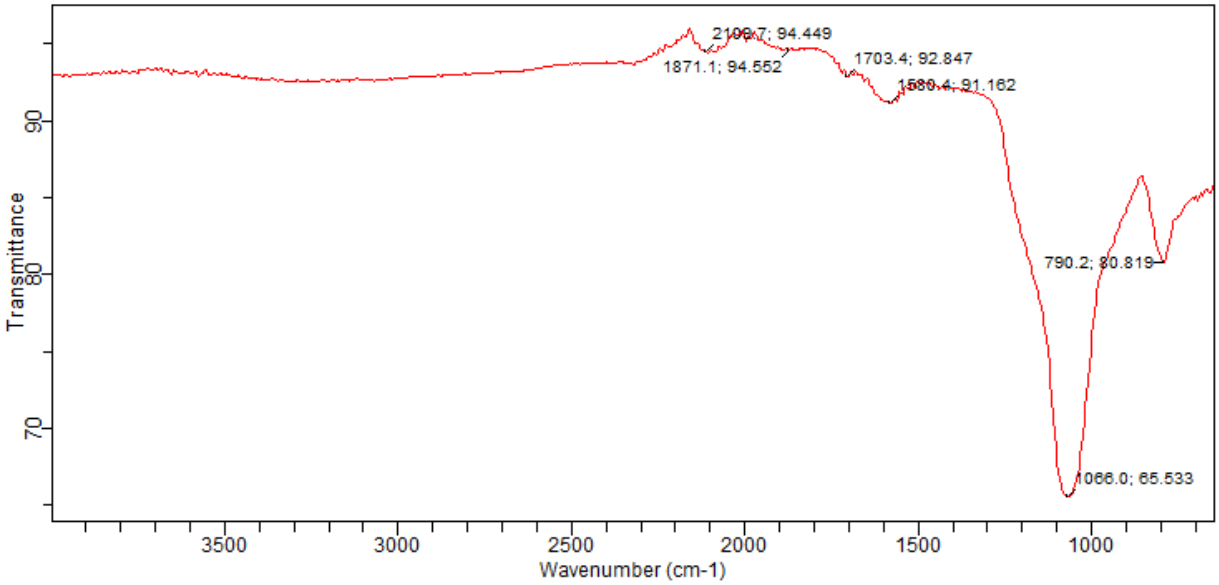

Fig3.3.1 FTIR spectrum for Al2O3 Nano composite before adsorption

From 908, 808, 780 cm^{-1} (strong fingerprint region) – Characteristic Al–O is stretching modes of tetrahedral and octahedral Al–O units, typical of transition-alumina (γ/δ/θ-Al_2O_3). These confirm the presence of the alumina network.
The strong bands between ~950–700 cm^{-1} are diagnostic for Al–O linkages and verify successful formation of an Al_2O_3 framework in the nanocomposite.The absence (or very weak presence) of a broad O–H band near 3400 cm^{-1} suggests effective calcination/dehydroxylation, i.e., relatively few surface hydroxyls remain—consistent with γ-Al_2O_3 after heat treatment.Residual C–H and C=O features indicate small amounts of organic species still on the surface, which is common for nanocomposites made with organic templates; these groups can modulate surface acidity/basicity and act as sites for adsorbate interaction.Taken together, the spectrum reflects a primarily alumina matrix with minor organic/adsorbed species, suitable for applications where Lewis acidic Al centers and tunable surface chemistry (via remaining organics/water) are advantageous—e.g., adsorption or catalysis.
Overall, the spectrum verifies the successful formation of an alumina framework, with the fingerprint region strongly supporting the Al–O lattice structure. The absence of a broad O–H band near 3400 cm^{-1} indicates that most hydroxyl groups were removed during calcination. However, minor signals from carbonyl and aliphatic groups suggest traces of organic residues remain, which may influence surface reactivity. This combination of features makes the nanocomposite suitable for adsorption and catalytic applications.
Analysis of BET
BET particle size distribution of Al_2O_3 nanocomposite before adsorption was shown in (Fig. 3.4.0). The distribution profile showed that the particles were mainly within the nanometer range and confirmwd the nanoscale nature of the material. A dominant peak was observed around the

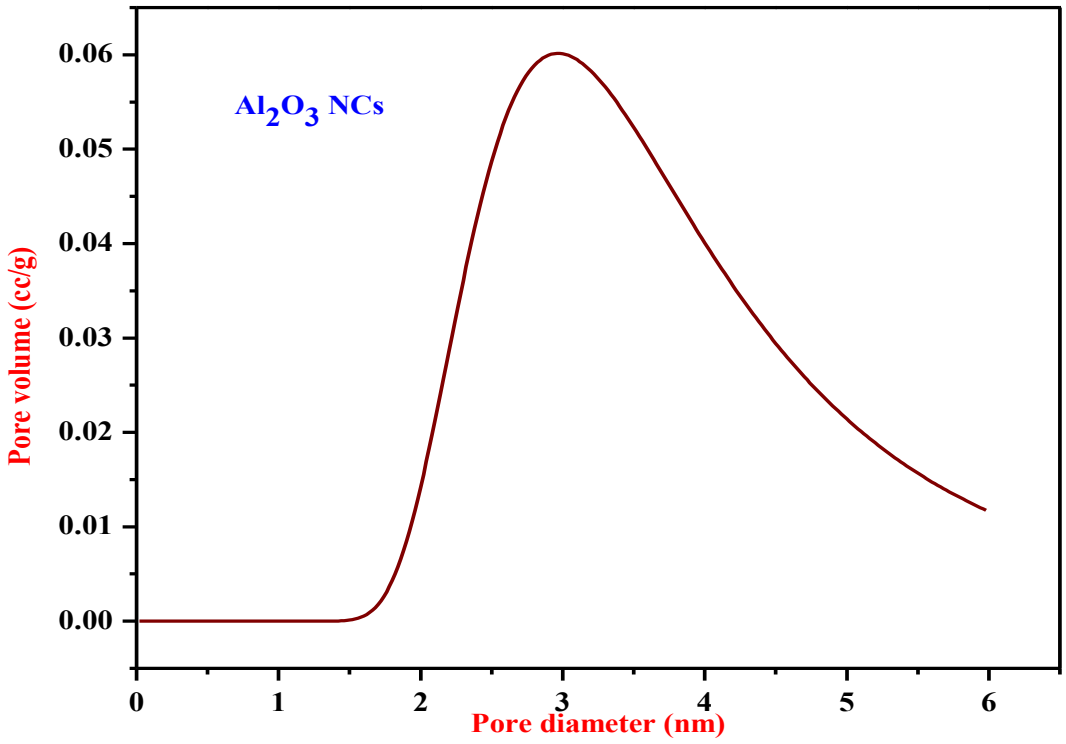

Fig 3.4.0 Particle Distribution of Al2O3 Nanocomposite

average particle diameter which indicated relatively a uniform particle size distribution. The curve exhibited slight broadening which suggested a minor agglomeration due to particle–particle interactions.

The measured average particle size and narrow distribution range indicated effective dispersion of Al_2O_3 nanoparticles within the activated carbon matrix. The absence of larger particle fractions further confirmed good homogeneity of the composite prior to adsorption.

Overall, the BET results demonstrated that the Al_2O_3 nanocomposite possessed nanoscale particle size, moderate uniformity, and suitable surface characteristics before adsorption.

Table 3.3. Showed that BET surface analysis of Al_2O_3 nanocomposite possessed a relatively high specific surface area, with values of about 190–200 $m^2\ g^{-1}$ obtained from the MPBP, MPB, BJH, and DR models. The DFT method gave a lower surface area, which was attributed to differences in model assumptions and pore geometry sensitivity. The Langmuir model produced an excessively high value, indicating that monolayer adsorption was not fully representative of the heterogeneous surface of the adsorbent.

The pore volume ranged from 0.051 to 0.169 $cm^3\ g^{-1}$, ascertaining the presence of a well-developed porous structure. The BJH pore diameter values (2.15–2.96 nm) and the average pore width of 6.366

nm indicated that the Al_2O_3 nanocomposite was predominantly mesoporous. The lower confidence limit of pore width (1.766 nm) suggested the coexistence of smaller pores.

The adsorption energy values (0.680–4.084 kJ mol^{-1}) indicated that the adsorption process was mainly governed by physisorption. The Freundlich constant (n = 1.169) further confirmed favorable adsorption on a heterogeneous surface. High correlation coefficients (r 0.997) for the MPBP and MPB models demonstrated good fitting of the experimental data, while the lower r value obtained from the Langmuir model suggested limited applicability.

Table 3.3.BET surface for Al2O3 Nano Composite Before Adsorption

Table 3.3.BET surface for Al_2O_3 Nano Composite Before Adsorption

Adsorbent	Parameter	MPBP (a)	DAP(b)	BJH (c)	MPB (d)	LG (e)	DR (f)	DAM (g)	DFT (h)
Al2O3	Surface area(m2/g)	190.048		199.652	190.048	16645.350	195.244		42.375
	Pore size(nm)								
	Pore/micropore volume(vcm3/g)		0.169	0.097			0.069	0.169	0.051
	Best E(KJ/MOL)		0.680					0.680	
	Best n		1.169					1.000	
	Pore diameter(mode)(nm)		2.960e +00	2.153				2.960e+ 00	
	Slope	12.375			12.375	2.09242	-5.246e-01		
	Intercept	5.950e+00			5.950e+ 00	6.23712	1.682e-02		
	Correlation coefficient, r	0.997019			0.99701 9	0.796	0.9903		
	C constant	3.080			3.080				
	Average pore width(nm)						6.366		
	Adsorption energy(kl/mol)						4.084		
	Lower confidence limit(nm)								1.766
	Por width(mode)%								2.783
	Moving point Average								Off
	Fitting error								2.783

Therefore, the BET results confirmed that the Al_2O_3 nanocomposite exhibited high surface area, suitable pore structure, and favorable adsorption characteristics, supporting its effectiveness as an adsorbent material.

In Multi-point BET plot (N_2 adsorption, 0.05–0.35 p/p_0 linear region): The BET linear region chosen where p/p_0 typically lied between 0.05–0.30. The slope and intercept yielded the monolayer volume (Vm) and the BET C constant. A large Vm (and hence large calculated BET surface area) indicated many accessible adsorption sites. A high C constant (>100) suggested strong adsorbate–adsorbent interactions (polar/acidic sites), whereas low C (<50) indicated weaker interactions or heterogeneity.

Langmuir isotherm: Langmuir fit indicated degree of monolayer adsorption on homogeneous sites. Good fit (high R^2) suggested adsorption dominated by uniform surface sites. If Langmuir R^2 was lower than BET or Freundlich, the surface was likely heterogeneous or multilayer adsorption occurs.

DA & DR: DA (or D–A) micropore analysis was used to estimate micropore volume and characteristic energy useful when microporosity contributed significantly. DR gaves the mean

adsorption energy (E). E values helped distinguish physisorption ($E<8$ kJ•mol^{-1}) from chemisorption ($E>16$ kJ•mol^{-1}). DA plot linearity indicated validity of micropore model in the low relative-pressure region.

BJH : BJH used the desorption branch (or adsorption branch) to calculate mesopore size distribution (2–50 nm). The presence of a distinct peak in BJH showed dominant mesopore sizes; a broad distribution indicated hierarchical porosity.

DFT : DFT yielded a more accurate pore-size distribution across micro- and mesopore ranges, particularly in the <2 nm region where BJH is unreliable. A DFT curve resolving micropores confirmed microporosity found by DA/DR and clarified the fine structure of the pore network.

Area/Volume summary from BET + t-plot + DFT: Reported BET specific surface area (m^2•g^{-1}), total pore volume (cm^3•g^{-1} at p/p_0 0.99), micropore volume (from t-plot or DA), average pore diameter (4•V/A or from BJH/DFT) and Related each to expected adsorption performance (higher area & appropriate pore volume → greater uptake capacity; appropriate pore size → easier diffusion of target species).

Therefore, the nitrogen adsorption–desorption analyses indicated that the Al_2O_3 nanocomposite possessed a high specific surface area, a mixed micro/mesoporous texture and a pore-size distribution dominated by dominant pore range e.g., mesopores 2–50 nm. The combination of BET, Langmuir, DA, DR, BJH and DFT analyses provided consistent evidence that the material offers abundant adsorption sites and a pore architecture favourable for ion uptake.

Analysis of TGA

Fig. 3.5.0 showed TG–DTA curve of Al_2O_3 nanocomposite before adsorption. The TGA curve revealed multi-stage weight loss. The initial loss below 150 °C was attributed to removal of adsorbed moisture, while the subsequent gradual loss corresponded to decomposition of surface functional groups and partial degradation of the carbon matrix. Weight remained stable at higher temperatures and indicated a thermal stability of the Al_2O_3 component.

The DTA curve displayed an endothermic peak at low temperature due to moisture evaporation and a broad exothermic peak at higher temperature linked to carbon decomposition. No sharp peaks indicated an absence of major phase transformations.

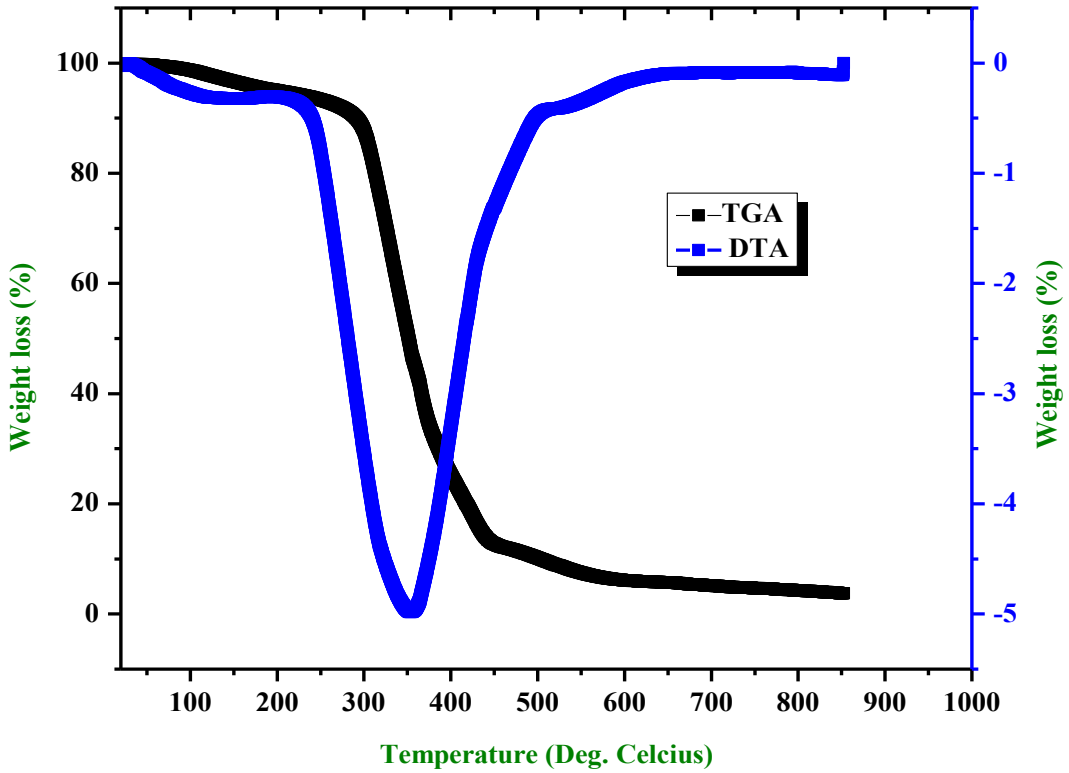

Fig 3.5.0 TG-DTA Curve of Al2O3 Nanocomposite

Overall, the analysis confirmed that the Al_2O_3 nanocomposite was thermally stable before adsorption, with weight loss primarily from moisture and carbonaceous decomposition, while the alumina framework remained intact.

Optimization of pH, Temprature, sonication time, initial concentration and dosage

Table 3.4. Illustrated the Central Composite Design (CCD) matrix applied to evaluate the influence of operating variables on the removal efficiency of Cd^{2+} ions using Al_2O_3 nanoparticle-loaded rice husk activated carbon. The studied independent variables included adsorbent dosage (0.2–1.0 g), initial Cd^{2+} ion concentration (100–900 mg/L), solution pH (3–11), and sonication time (10–50 min), while the response was Cd^{2+} removal efficiency (%).

The experimental design consisted of 30 runs incorporating factorial, axial, and replicated center points. The repeated center point experiments conducted at 0.6 g adsorbent dosage, 500 mg/L Cd^{2+} concentration, pH 7, and 30 min sonication time showed removal efficiencies ranging from 88.79% to 92.41%, confirming good experimental reproducibility and model reliability.

Cd^{2+} removal efficiency varied markedly across the experimental conditions indicated significant combined effects of the selected parameters. Higher removal efficiencies were generally obtained at moderate adsorbent dosage, near-neutral pH, and intermediate sonication time, which testified favorable adsorbent–adsorbate interactions and enhanced mass transfer. In contrast, lower efficiencies were observed at extreme pH values and shorter sonication times, likely due to reduced surface affinity, competition with hydrogen ions at low pH, and limited contact between Cd^{2+} ions and the adsorbent.

The predicted removal efficiencies closely agreed with the experimental values, with small and randomly distributed residuals, mostly within ±2%, demonstrating the adequacy and predictive accuracy of the CCD model. Furthermore, an increase in initial Cd^{2+} concentration beyond moderate levels resulted in decreased removal efficiency, which was attributed to saturation of available adsorption sites on the Al_2O_3 nanocomposite.

Taken together, the CCD analysis confirmed that adsorbent dosage, solution pH, initial Cd^{2+} concentration, and sonication time significantly influenced Cd^{2+} removal efficiency. The close correlation between observed and predicted responses validated the suitability of the CCD approach for modeling and optimizing the adsorption process at the MSc thesis level.

Fig.3.4.Illustrated ramp plot for the numerical optimization results obtained for Cd^{2+} adsorption onto the Al_2O_3 nanocomposite by simultaneously considering the selected independent variables and the desired response. Each ramp represented the individual effect of process parameters such as initial Cd^{2+} concentration, adsorbent dosage, contact time and solution pH on the adsorption efficiency within the investigated experimental ranges. The slopes of the ramps indicated the direction and extent to which each variable influenced the response, while the vertical dashed lines denoted the optimal levels of the factors selected by the optimization criteria.

At the optimized conditions, the desirability function approached unity, signifying that the chosen parameter combination effectively maximized Cd^{2+} adsorption efficiency. The response ramp showed that the predicted adsorption efficiency was close to its upper limit, confirming that the optimization goal was successfully achieved. The smooth and continuous nature of the ramps suggested that the model adequately captured the interaction between variables without abrupt changes or instability.

Taken together, the ramp plot confirmed that the numerical optimization procedure successfully identified the most favorable operating conditions for Cd^{2+} adsorption onto the Al_2O_3 nanocomposite. The optimized parameter settings were therefore considered reliable and suitable for achieving maximum adsorption efficiency within the studied experimental domain.

Fig.3.5. 3D and contour response surface plots of interactive effects of (a) pH and amount of adsorbent (b) Metal ion concentration and amount of adsorbent (c) Sonication time and pHon Cd2+ adsorption onto Al2O3 nanocomposite.

(3.51a) pH and adsorbent dosage: The 3D and contour plots showed that Cd^{2+} adsorption efficiency increased with increasing pH and adsorbent dosage up to their optimum levels. This behavior was attributed to reduced H^+ competition and the availability of more active sites at higher dosages. The elliptical contour patterns indicated a significant interaction between pH and adsorbent dosage.

(3.51b) Initial Cd^{2+} concentration and adsorbent dosage: The response surfaces revealed that adsorption efficiency improved with increasing adsorbent dosage but decreased at higher initial Cd^{2+} concentrations due to saturation of adsorption sites. The contour plots confirmed a notable interaction, where higher dosages mitigated the effect of increased metal ion concentration.

(3.51c) Sonication time and pH: The plots indicated that Cd^{2+} adsorption increased with sonication time and pH up to optimum values, owing to enhanced mass transfer and favorable surface charge conditions. The curved surfaces and elliptical contours confirmed a significant interaction between sonication time and pH.

Taken together, the response surface plots demonstrated the combined influence of the studied variables and confirmed the adequacy of the model in describing Cd^{2+} adsorption onto the Al_2O_3 nanocomposite.

Table 3.4.Central Composite Design Matrix for the response of Cd2+ Removal Efficiency by Al2O3nanoparticle-loaded rice husk activated carbon

Table 3.4. Central Composite Design Matrix for the response of Cd^{2+} Removal Efficiency by Al_2O_3nanoparticle-loaded rice husk activated carbon

Run	Amount of Adsorbent (g)	Pb^{2+} Ion Conc. (mg/L) C_o	pH	Sonication Time (min)	Observed R %	Predicted R %	Residual
1	0.6	500	7	30	90.67	89.99	0.68
2	0.6	500	7	30	89.04	89.99	-0.95
3	0.4	300	5	40	89.49	90.15	-0.66
4	0.6	500	7	10	72.52	74.19	-1.67
5	0.4	300	5	20	87.94	87.55	0.39
6	0.4	700	5	20	82.65	81.31	1.34
7	0.8	300	9	40	76.31	77.2	-0.89
8	1	500	7	30	78.23	78.65	-0.42
9	0.4	700	9	40	76.31	77.13	-0.82
10	0.6	500	3	30	76.37	77.78	-1.41
11	0.2	500	7	30	90.21	89.15	1.06
12	0.4	700	9	20	79.88	80.06	-0.18
13	0.6	500	11	30	71.45	69.4	2.05
14	0.8	700	9	20	76.49	75.38	1.11
15	0.8	700	5	20	74.16	74.08	0.08
16	0.6	500	7	30	90.07	89.99	0.08
17	0.6	100	7	30	89.46	88.14	1.32
18	0.6	900	7	30	81.94	82.62	-0.68
19	0.4	300	9	40	79.31	80.47	-1.16
20	0.8	300	9	20	72.44	72.8	-0.36
21	0.6	500	7	30	92.41	89.99	2.42
22	0.8	700	5	40	81.66	80.27	1.39
23	0.8	700	9	40	76.44	77.92	-1.48
24	0.8	300	5	20	77.53	76.26	1.27
25	0.6	500	7	30	88.98	89.99	-1.01
26	0.8	300	5	40	83.42	84.33	-0.91
27	0.6	500	7	30	88.79	89.99	-1.2
28	0.4	300	9	20	80.59	81.53	-0.94
29	0.4	700	5	40	81.32	82.04	-0.72
30	0.6	500	7	50	81.63	79.32	2.31

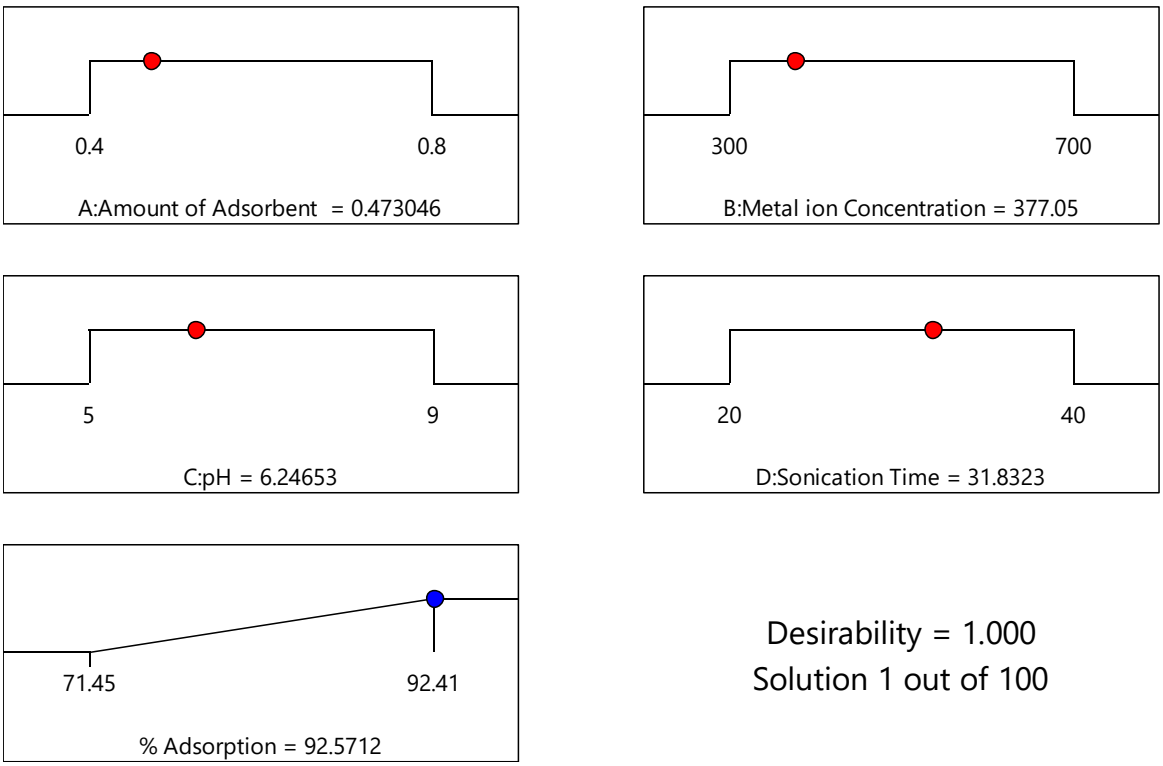

Fig.3.4. Ramp plot of numerical optimization of Cd2+ adsorption onto Al2O3 nanocomposite

(a)

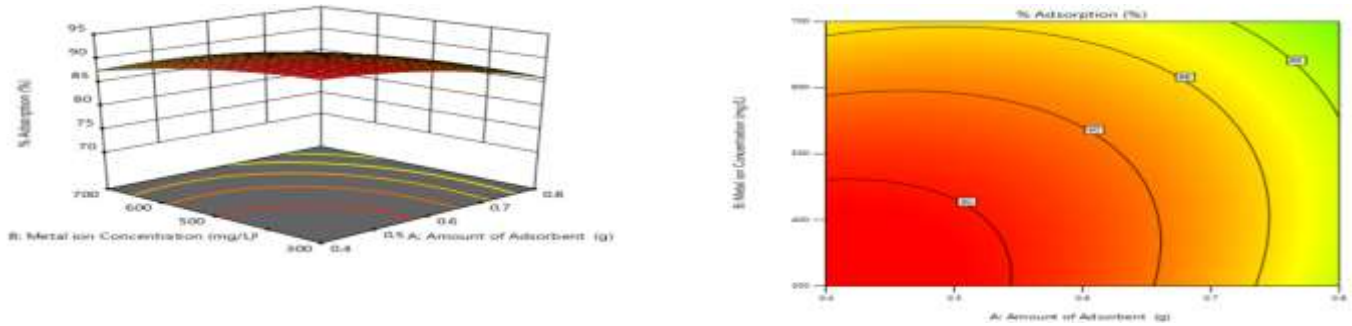

(b)

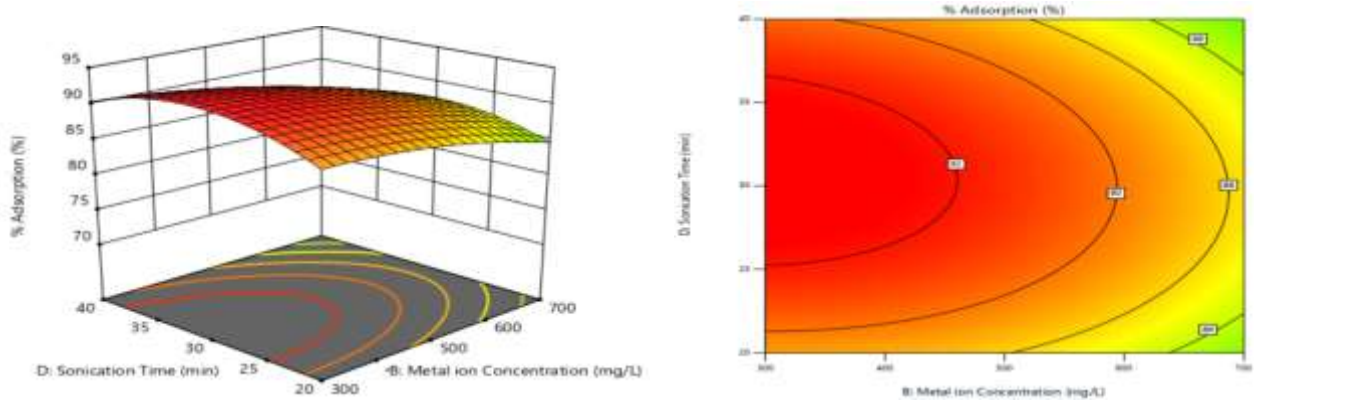

(c)

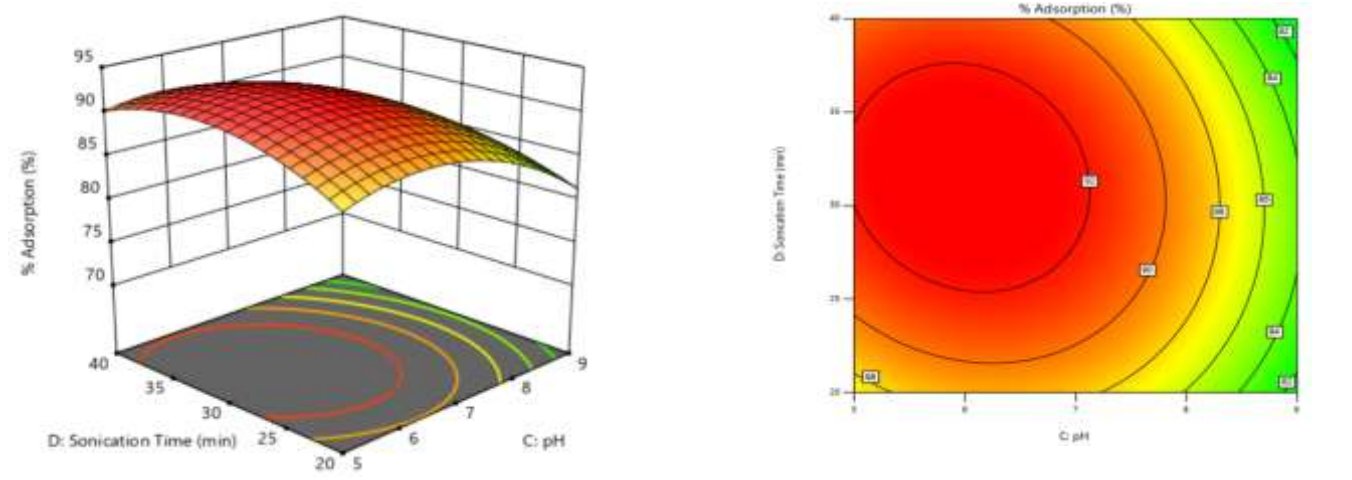

Fig.3.51. 3D and contour response surface plots of interactive effects of (a) pH and amount of adsorbent (b)Metal ion concentration and amount of adsorbent (c) Sonication time and pHon Cd2+ adsorption onto Al2O3 nanocomposite.

Isotherm Models

Fig. 3.6. showed Langmuir plot of linear relationship between C_e and q_e, which indicated monolayer adsorption of Cd^{2+} onto a homogeneous surface with finite, uniform active sites. The slope and intercept provided the maximum adsorption capacity (qm) and the Langmuir constant (K-L), reflecting the adsorbent's capacity and affinity. A high correlation coefficient confirmed the suitability of the model.

Conversely, the plot demonstrated that Cd^{2+} adsorption followed the Langmuir model, highlighting the effectiveness of the Al_2O_3 nanocomposite for monolayer adsorption under the studied conditions.

Fig. 3.7. showed a Freundlich plot of linear relationship between ln q_e and ln C_e, indicating multilayer adsorption on a heterogeneous surface with sites of varying energies. The slope (1/n) reflected adsorption intensity, while the intercept (ln K-F) represented the adsorption capacity. A high R^2 value confirmed a good fit of the model to the experimental data, and $1/n < 1$ indicated favorable adsorption. The plot confirmed that Cd^{2+} adsorption was favorable, occurred on a heterogeneous surface, and demonstrated the effectiveness of the Al_2O_3 nanocomposite for multilayer adsorption.

Fig. 3.8. showed a Temkin plot of linear relationship between q_e and ln C_e, indicating that the heat of adsorption decreased gradually with increasing surface coverage. The slope represented the Temkin constant (B), reflecting adsorption heat, while the intercept provided the equilibrium

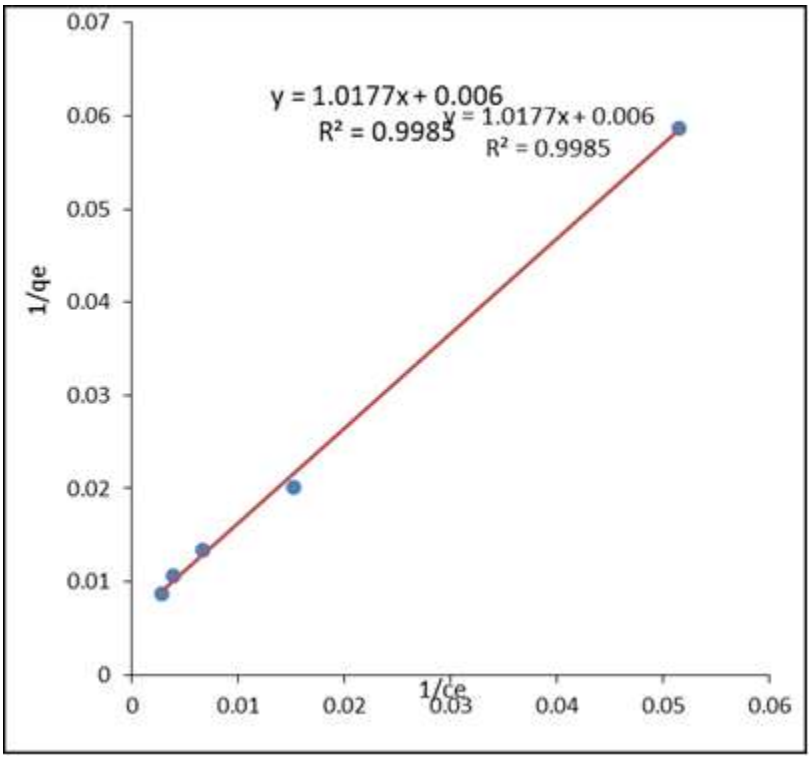

Fig.3.6. Longmuir isotherm plot for adsorption of Cd2+ on Al2O3 nanocomposite

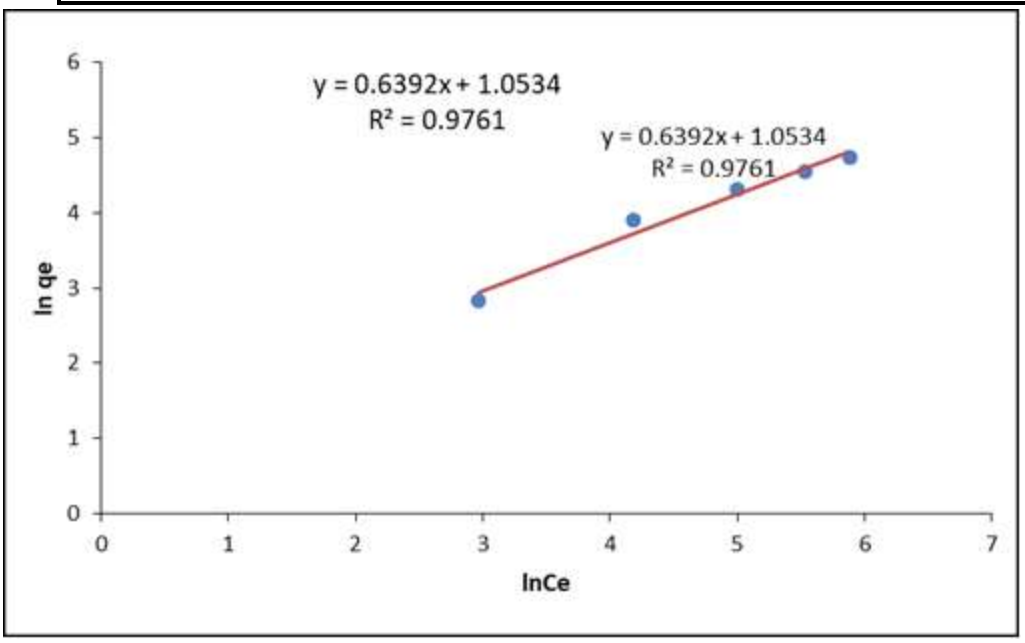

Fig. 3.7. Freundlich isotherm for adsorption of Cd2+ on Al2O3 nanocomposite

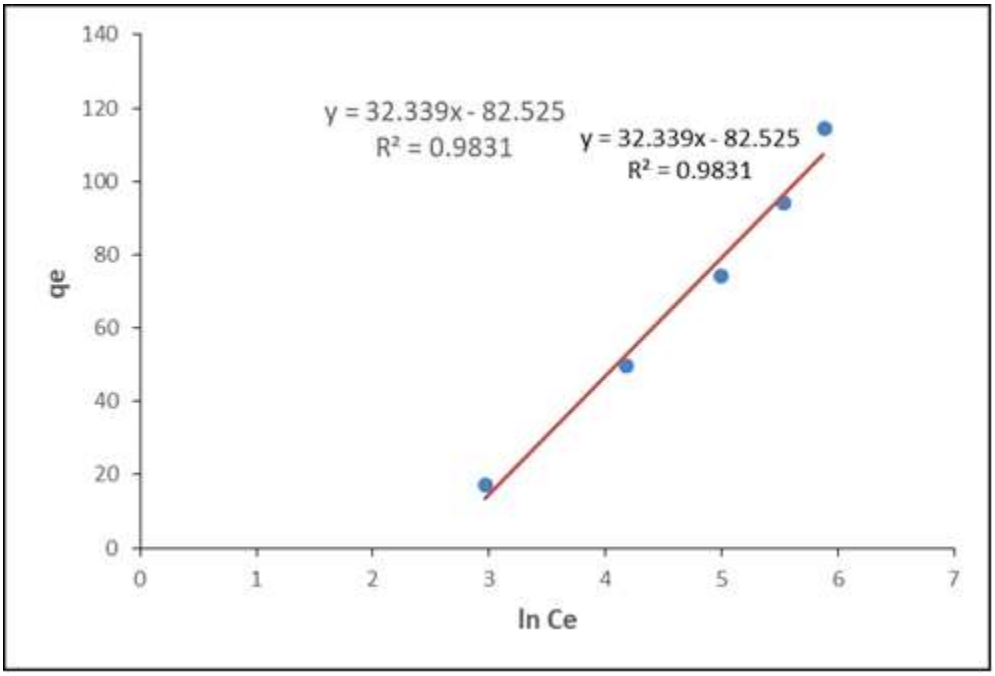

Fig. 3.8. Temkin isotherm plot for the adsorption of Cd2+ on Al2O3 nanocomposite

binding constant (A-T), representing adsorbent–adsorbate interaction strength. A high R^2 value confirmed a good fit of the model to the experimental data.

Therefore, the plot suggested that Cd^{2+} adsorption was influenced by adsorbent–adsorbate interactions under moderate surface coverage and confirmed the efficiency of the Al_2O_3 nanocomposite for Cd^{2+} removal.

Table 3.5.Presented the isotherm parameters obtained from fitting the experimental Cd^{2+} adsorption data to the Langmuir, Freundlich, and Temkin models.

The Langmuir isotherm showed a maximum adsorption capacity (qmax) of 166.667mg/g and a Langmuir constant (b) of 0.00589 L/mg, indicating strong affinity of the adsorbent for Cd^{2+} ions. The separation factor (R-L = 0.3105) suggested favorable adsorption. A high R^2 value of 0.9985 confirmed that the adsorption process predominantly followed monolayer coverage on a homogeneous surface.

The Freundlich isotherm yielded a Freundlich constant (K-f) of 2.867L/mg and an adsorption intensity parameter 1/n of 0.6392 (n = 1.564), indicating favorable multilayer adsorption on a heterogeneous surface. The model showed good agreement with the experimental data (R^2 = 0.9761), though slightly lower than the Langmuir fit.

The Temkin isotherm gave an equilibrium binding constant (A) of 0.0779L/mg and a Temkin constant (B) of 32.339, corresponding to a heat of adsorption (b) of 30.022J/mol. The R^2 value of 0.9831 indicated that adsorbent–adsorbate interactions influenced adsorption and that the heat of adsorption decreased linearly with surface coverage.

Overall, the R^2 comparison suggested that Cd^{2+} adsorption was best described by the Langmuir model, confirming monolayer adsorption, while Freundlich and Temkin models highlighted surface heterogeneity and adsorbent–adsorbate interactions. The high qmax and favorable

Table 3.5.Isotherm parameters related to the adsorption ofCd2+adsorptionontoAl2O3nanoparticle-loaded rice husk activated carbon

Table 3.5. Isotherm parameters related to the adsorption ofCd^{2+}adsorptionontoAl_2O_3nanoparticle-loaded rice husk activated carbon

Isotherm Model	Regression Equation	Isotherm parameters	Value
Langmuir	y = 1.0177x + 0.006	q_{max}(mg/g)	166.667
		b(L/mg)	0.00589
		R_L	0.3105
		R^2	0.9985
Freundlich	y = 0.6392x + 1.0534	K_f(L/mg)	2.867
		$1/n$	0.6392
		n	1.564
		R^2	0.9761
Temkin	y = 32.339x - 82.525	A(L/mg)	0.0779
		B	32.339
		$b(J/mol)$	30.022
		R^2	0.9831

isotherm constants demonstrated the effectiveness of the Al_2O_3 nanoparticle-loaded rice husk activated carbon for Cd^{2+} removal.

Kinetics Study

Fig. 3.9. showed a pseudo-first-order plot of linear relationship between ln (qe−qt) and time (t) for Cd^{2+} adsorption. The slope represented the pseudo-first-order rate constant (k_1), and the intercept corresponded to ln qe.

Although a linear trend was observed, the correlation coefficient (R^2) was relatively low, indicating that the pseudo-first-order model did not adequately describe the adsorption process. The model underestimated the equilibrium adsorption capacity (qe), suggesting that physical adsorption alone did not govern the process.

Generally, the pseudo-first-order kinetics partially described Cd^{2+} adsorption but was less suitable than the pseudo-second-order model, implying that chemisorption and other rate-controlling mechanisms played a dominant role.

Fig.3.10. showed the pseudo-second-order kinetic plot for Cd^{2+} adsorption onto Al_2O_3 nanocomposite. The data fitted the model well, with a high R2value, indicating chemisorption as the dominant mechanism. The calculated equilibrium adsorption capacity (qe) closely matched the experimental values, and the rate constant (k2) reflected rapid adsorption to the available sites. Overall, the model accurately described the adsorption kinetics and confirmed the reliability of the experimental data.

Fig.3.11. Showed the intra-particle diffusion plot for Cd^{2+} adsorption onto Al_2O_3 nanocomposite. The plot exhibited multiple linear regions, indicating that adsorption occurred in stages: rapid surface adsorption followed by slower intra-particle diffusion. The non-zero intercept (C) suggested that diffusion within pores was not the sole rate-limiting step, and boundary layer

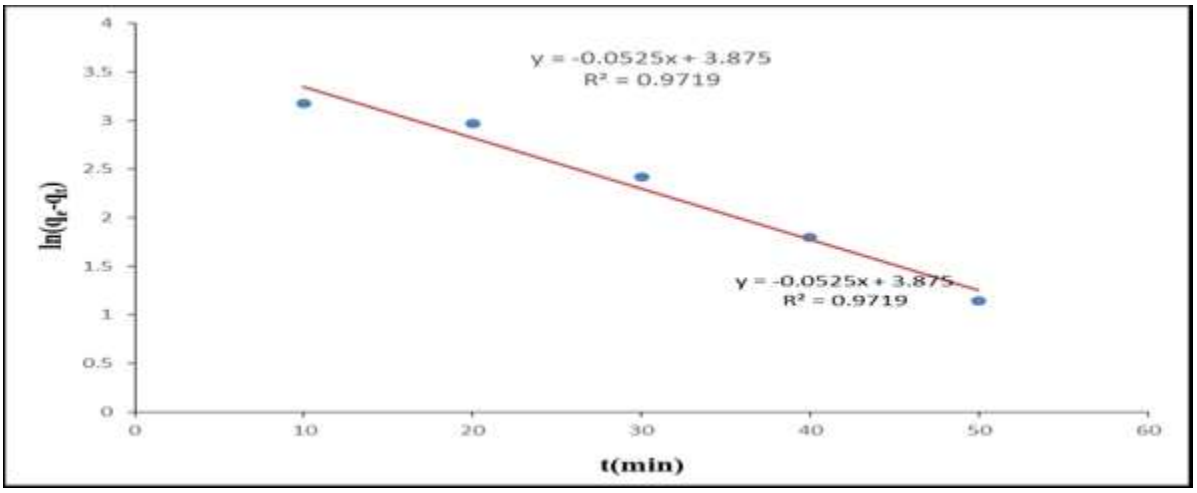

Fig.3. 9. Pseudo-first-order plot of Cd^{2+} adsorptionon Al_2O_3 nanocomposite.

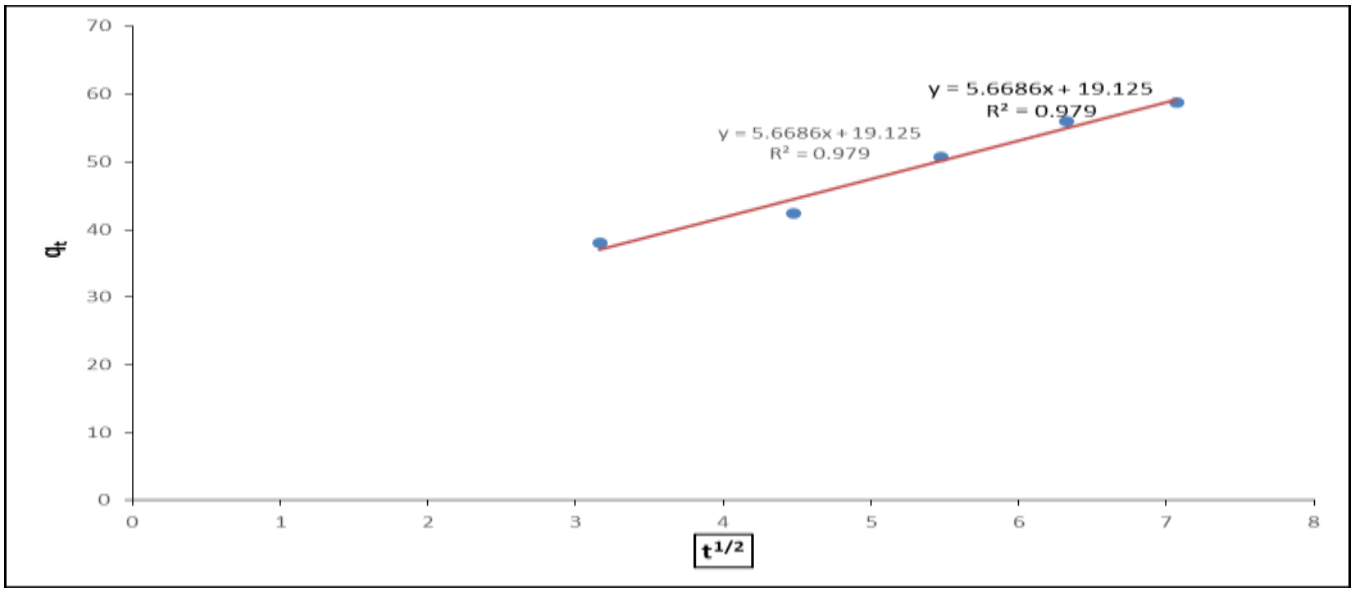

Fig 3. 11. Intra-particle diffusion kinetic model plot for the adsorption ofCd2+ on Al2O3 nanocomposite

effects also contributed. The high R2 value confirmed the model's reliability, highlighting that intra-particle diffusion controlled the later stage of adsorption while chemisorption dominated initially

Table 3.6.Summarized the kinetic parameters for Cd^{2+} adsorption onto Al_2O_3 nanoparticle-loaded rice husk activated carbon. The pseudo-second-order model best described the adsorption process, with a calculated qeclosely matching the experimental value and a high R2of 0.987, indicating chemisorption as the dominant mechanism. The pseudo-first-order model showed a lower R2 (0.972) and a larger deviation between calculated and experimental capacities, suggesting a less accurate fit. Intra-particle diffusion contributed to the later stage of adsorption, as indicated by a non-zero intercept (C=19.13mg/g) and R2=0.979, implying that both surface adsorption and pore diffusion influenced the overall process. Overall, Cd^{2+} adsorption occurred in stages, with chemisorption controlling the initial phase and intra-particle diffusion affecting the subsequent rate.

Thermodynamics study

Figure 3. 12. presented Van't Hoff plot for Cd^{2+} adsorption onto Al_2O_3 nanoparticle-loaded rice husk activated carbon. The linear relationship between InK and 1/T, together with a high R2 value, confirmed the suitability and reliability of the thermodynamic model. The positive slope of the plot yielded a positive standard enthalpy change (ΔH°=33.985kJ mol^{-1}), indicating that the adsorption process was endothermic. The positive intercept corresponded to a positive entropy change (ΔS°=0.116 kJ mol^{-1} K^{-1}), suggesting an increase in randomness at the solid–solution interface during adsorption. Furthermore, the progressively more negative Gibbs free energy values (ΔG°) with increasing temperature confirmed that Cd^{2+} adsorption was spontaneous and

Table 3.6. Kinetic parameters related to various models for the adsorption of Cd^{2+}adsorptionon Al_2O_3 nanoparticle-loaded rice husk activated carbon

Kinetic Model	Kinetic parameter	Value
Pseudo-first-order	$q_{e\,exp}(mg.g^{-1})$	61.942
	$q_{e\ cal}(mg.g^{-1})$	48.183
	$q_{e\,exp} - q_{e\ cal}(mg.g^{-1})$	13.759
	$k_1(\text{min}^{-1})$	0.0525
	R^2	0.9719
Pseudo-second-order	$q_{e\ cal}(mg.g^{-1})$	70.423
	$q_{e\ cal} - q_{e\,exp}(mg.g^{-1})$	8.481
	$k_2(g.mg^{-1}\text{min}^{-1})$	0.00132
	R^2	0.9873
Intra-particle diffusion	$k_{id}(mg.g^{-1}.min^{-1/2})$	5.6686
	$C(mg.g^{-1})$	19.125
	R^2	0.979

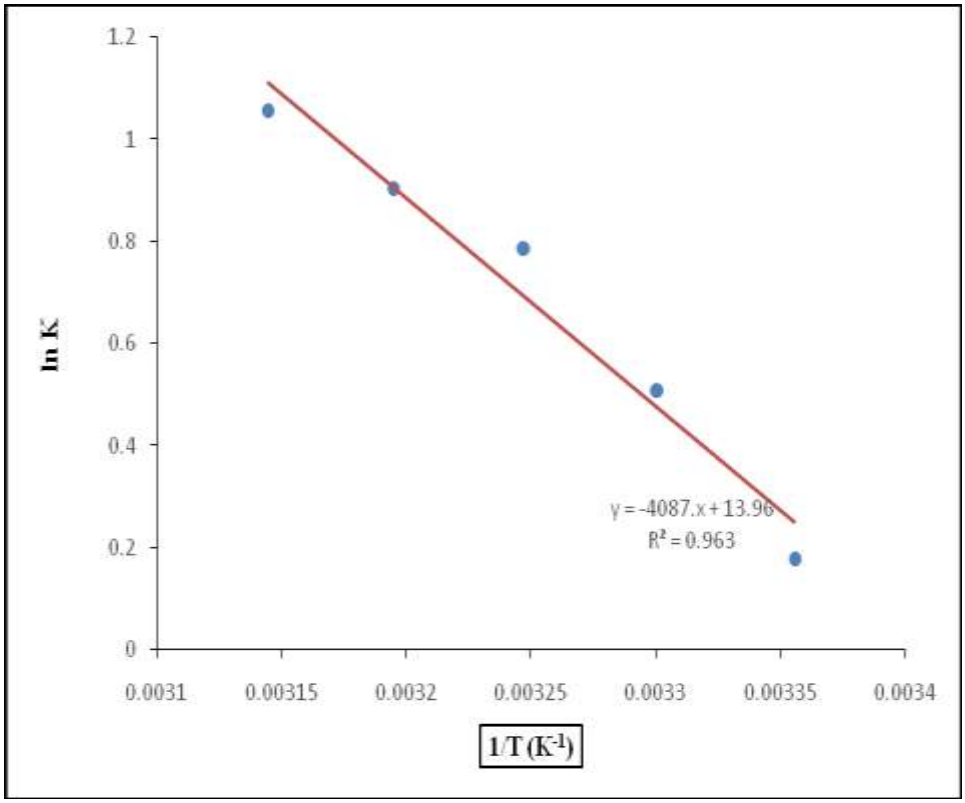

Fig. 3.12. Van't Hoff plot for the adsorptionof Cd2+adsorptionon Al2O3nanoparticle-loaded rice husk

increasingly favored at higher temperatures. Overall, the Van't Hoff plot demonstrated that the adsorption process was spontaneous, endothermic, and entropy-driven.

Table 3.7. Summarized the thermodynamic parameters for Cd^{2+} adsorption onto Al_2O_3 nanoparticle-loaded rice husk activated carbon within the temperature range of 298–318 K. The equilibrium constant (K) increased from 1.196 to 2.874 with increasing temperature, accompanied by a corresponding rise in InK values, indicating improved adsorption favorability at elevated temperatures.

The standard Gibbs free energy change (ΔG°) values were negative at all temperatures (−0.583 to −2.903 kJ mol^{-1}), confirming that the adsorption process was spontaneous and became more favorable as temperature increased. The positive standard enthalpy change (ΔH° = 33.985 kJ mol^{-1}) demonstrated that the adsorption process was endothermic, which was consistent with the enhanced adsorption observed at higher temperatures.

The positive standard entropy change (ΔS° = 0.116 kJ mol^{-1} K^{-1}) indicated an increase in randomness at the solid–liquid interface during adsorption, likely due to the displacement of water molecules by Cd^{2+} ions. Overall, the thermodynamic parameters confirmed that Cd^{2+} adsorption onto the Al_2O_3 nanocomposite was spontaneous, endothermic, and thermodynamically favorable, supporting its potential application in aqueous Cd^{2+} removal.

Table 3.7. Thermodynamic parameters of Cd2+adsorptionon Al2O3nanoparticle-loaded rice husk activated carbon

Table 3.7. Thermodynamic parameters of Cd^{2+}adsorptionon Al_2O_3nanoparticle-loaded rice husk activated carbon

Run	T (℃)	T(K)	1/T (K^{-1})	K	lnK	ΔH^o $kJmol^{-1}$	ΔS^o $kJmol^{-1}$	ΔG^o $kJmol^{-1}$
1	25.000	298.000	0.00336	1.196	0.1786			-0.583
2	30.000	303.000	0.0033	1.662	0.5083			-1.163
3	35.000	308.000	0.00325	2.195	0.7861	33.985	0.116	-1.743
4	40.000	313.000	0.00319	2.467	0.903			-2.323
5	45.000	318.000	0.00314	2.874	1.0557			-2.903

CONCLUSION

By conclusion, 226.7 g Rice husk activated carbon was successfully prepared from 1200 g of precursor, with a percentage yield of 19% which showed asignificant mass loss during carbonization and activation. The 25 g (5%) Al_2O_3 nanocomposite synthesized from 504.3 g aluminium sulphate indicated greater mass loss during Al_2O_3 formation. Adsorption of Cd^{2+} on Al_2O_3 nanocomposite was systematically investigated through characterization, optimization, isotherm, kinetics, and thermodynamics studies. Characterization showed that Al_2O_3 nanocomposite had higher surface area and active sites which inhanced higher adsorption. Optimization revealed significant effects of adsorbent dosage (0.6 g), metal ion concentration (500 mg/L), pH7, and contact/sonication time (30 min) by achieving maximum removal efficiencies of 92.4% (Cd^{2+}/Al_2O_3). Langmuir isotherm best described all systems and confirmed monolayer adsorption, while kinetics followed pseudo-second-order models which indicated chemisorption with intra-particle diffusion to influence later stages. Thermodynamics confirmed spontaneous, endothermic, and entropy-driven processes (ΔG° = −0.58 to −2.903 kJ/mol; ΔH° = 33.99 kJ/mol; ΔS° = 0.116 kJ/mol•K).

REFERENCES

Ahmed, S. A.(2019) Batch and Fixed-Bed Column Techniques for Removal of Cu(II) and Fe(III) Using Carbohydrate Natural Polymer Modified Complexing Agents. Carbohydr. Polym., 83, 1470– 1478, DOI: 10.1016/j.carbpol.2010.09.051

Akponikpe, P., Wima, K., Yakouba, H., & Mermoud, A. (2021). Reuse of domestic wastewater treated in macrophyte ponds to irrigate tomato and eggplants in semi-arid West-Africa: Benefits and risks. Agricultural Water Management, 98, 834–840.

Alghobar, M. A., Ramachandra, L., & Suresha, S. (2019). Effect of sewage water irrigation on soil properties and evaluation of the accumulation of elements in Grass crop in Mysore city, Karnataka, India. American Journal of Environmental Protection, 3, 283–291.

Atieh, M. A., Ji, Y. & Kochkodan, V.(2017) Metals in the environment: Toxic metals cause serious in every environment. Journal of Preventive Medicine and Public Health, 43, 74–85.

Dada A.O., Ojediran J.O., Olalekan A.P. (2022). Sorption of Pb2+ from aqueous solution unto modified rice husk: isotherms studies. Adv. Phys. Chem.;2013:1–7. 842425.

Dickin, S. K., Schuster-Wallace, C. J., Qadir, M., & Pizzacalla, K. (2017). A review of health risks and pathways for exposure to wastewater use in agriculture. Environmental Health Perspectives, 124, 900–909.

Efome, J. E.; Rana, D.; Matsuura, T.; Lan, C. Q.(2018) Insight Studies on Metal-Organic Framework Nanofibrous Membrane Adsorption and Activation for Heavy Metal Ions Removal from Aqueous Solution. ACS Appl. Mater. Interfaces, 10, 18619– 18629, DOI: 10.1021/acsami.8b01454

Ekpete O.A., Horsfall M., Harcourt P., Chemistry I., Harcourt P. (2020). Preparation and characterization of activated carbon derived from fluted pumpkin stem waste (Telfairia occidentalis Hook F) Res. J. Chem. Sci.;1:10–17.

Fraser-Quick, G. (2022). Vermiculture – A sustainable total waste management solution. What's New in Waste Management?, 4, 13–16.

Giddins, M. J., Macesic, N., Annavajhala, M. K., Stump, S., Khan, S., McConville, T. H., Mehta, M., Gomez-Simmonds, A., & Uhlemann, A. C. (2017). Successive emergence of ceftazidime-avibactam resistance through distinct genomic adaptations in bla(KPC-2)-harboring Klebsiella pneumoniae sequence type 307 isolates. Antimicrobial Agents and Chemotherapy, 62, e02101–e02117.

Gilchrist, J. D. (2019), extraction metalliergy (3rd ed). Oxford: pergamon press. P. 145.ISBN 0-08 036612-0.

Li, H.; Wang, F.; Li, J.; Deng, S.; Zhang, S. (2021). Adsorption of Three Pesticides on Polyethylene Microplastics in Aqueous Solutions: Kinetics, Isotherms, Thermodynamics, and Molecular Dynamics Simulation. Chemosphere, 264, 128556, DOI:10.1016/j.chemosphere.2020.128556

Li, Y.; Yang, L.; Xu, Z.; Sun, Q.(2017) Separation and Recovery of Heavy Metals from Waste Water Using Synergistic Solvent Extraction. IOP Conf. Ser. Mater. Sci. Eng., 167, 012005 DOI: 10.1088/1757-899X/167/1/012005

Leddy, M. B., Plumlee, M. H., Kantor, R. S., Nelson, K. L., Miller, S. E., Kennedy, L. C., et al. (2018). High-throughput DNA sequencing to profile microbial water quality of potable reuse. Water online, 1-4.

Mahmood, A., & Malik, R. N. (2019). Human health risk assessment of heavy metals via consumption of contaminated vegetables collected from different irrigation sources in Lahore. Pakistan, Arabian Journal of Chemistry, 7(1), 91–99.

Mahdieh M. H. and Fattahi B. (2022) "Size properties of colloidal nanoparticles produced by nanosecond pulsed laser ablation and studying the effects of liquid medium and laser fluence," Applied Surface Science, vol. 329, pp. 47–57, 2015.

Mehmood, A., Mirza, A. S., Choudhary, M. A., Kim, K. H., Raza, W., Raza, N., Lee, S. S., Zhang, M., Lee, J. H., & Sarfraz, M. (2019). Spatial distribution of heavy metals in crops in a wastewater irrigated zone and health risk assessment. Environmental Research, 168, 382–388.

Mousavi, S.Y. (2021). Mechanical properties and durability assessment of rice husk ash concrete, Biosystems Engineering, 110(2), 144-152.

Mubita, T. M.; Dykstra, J. E.; Biesheuvel, P. M.; van der Wal, A.; Porada, S. (2019). Selective Adsorption of Nitrate over Chloride in Microporous Carbons. Water Res., 164, 114885, DOI: 10.1016/j.watres.2019.114885.

Maji S.K., pal, A., pal, t., adak, A. (2018). modeling and fixed bed column adsorption 0f Cu (11) on laterite soil. Saparation and purification technology. 56(3): 284-290. [doi: 10.1016/j. seppur. 2007. 02,011].

Masindi, V. & Muedi, K. L. (2018).Environmental Contamination by Heavy Metals, Heavy Metals, HosamElDinM.SalehandRefaatF.Aglan,IntechOpen.https://doi.org/10.5772/intechopen.76082

Masoudian N., Rajabi M., Ghaedi M. (2019). Titanium oxide nanoparticles loaded onto activated carbon prepared from bio-waste watermelon rind for the efficient ultrasonic-assisted adsorption of Congo red and phenol red dyes from wastewaters. Polyhedron.;173.

Mchenry, C., ed (2017). The new encyclopedia Britannica. 3 (15 ed.). Chicago: encyclopedia Britannica inc. p.612. ISBN 0-85229- 553 -7.

Ojediran J.O., Dada A.O., Aniyi S.O., David R.O. (2020 $ 2022)Functionalized Zea Mays Cob (FZMC) as low-cost agro-waste for effective adsorption of malachite green dyes data set. Chem. Data Collect.; 30.

Okewale, A. & Omoruwuo, F. (2018) Neem leaf extract as a corrosion inhibitor on mild steel inacidicsolution. Int. J. Eng. Res. Africa 35,208220.
https://doi.org/10.4028/www.scientific.net/JERA.35.208.

Qadir, M., Wichelns, D., Raschid-Sally, L., McCornick, P. G., Drechsel, P., Bahri, A., et al. (2020). The challenges of wastewater irrigation in developing countries. Agricultural Water Management, 97, 561–568.

Rafatullah, M.; Sulaiman, O.; Hashim, R.; Ahmad, A. (2019) Adsorption of Methylene Blue on Low-Cost Adsorbents: A Review. J. Hazard. Mater. , 177 (1–3), 70– 80, DOI: 10.1016/j.jhazmat.2009.12.047

Rajput V.D., and Yaning C. (2023). Biosorption of heavy metals using agrowaste: a review. Pollut. Res. Pap.;34(1):34–38.

Ramseur, Jonathan L., (September 22,2017). Waste water infrastracture: overview funing and legislative development (PDF). Washington DC: congressional research service retrived 17 december 2017.

Ramasamy, V. (2021). Compressive Strength and Durability Properties of Rice Husk Ash Concrete, KSCE Journal of Civil Engineering, 16(1),93-102.

Shakir, R., Davis, S., Norrving, B., Grisold, W., Carroll, W. M., Feigin, V., & Hachinski, V. (2017). Revising the ICD: Stroke is a brain disease. Lancet, 19, 2475–2476.

White B.R., Stackhouse B.T., Holcombe J.A. (2019). Magnetic γ-Fe2O3 nanoparticles coated with poly-l-cysteine for chelation of As(III), Cu(II), Cd(II), Ni(II), Pb(II) and Zn(II) J. Hazard Mater. 2009;161:848–853.